Biochimica et Biophysica Acta 1838 (2014) 3061–3068

Contents lists available at ScienceDirect

Biochimica et Biophysica Acta

journal homepage: www.elsevier.com/locate/bbamem

Structural dynamics of the cell wall precursor lipid II in the presence and absence of the lantibiotic nisin

Dennis C. Koch [a], Thomas H. Schmidt [a], Hans-Georg Sahl [b], Ulrich Kubitscheck [c], Christian Kandt [a,*]

[a] Computational Structural Biology, Department of Life Science Informatics B-IT, Life & Medical Sciences (LIMES) Institute, Rheinische Friedrich Wilhelms-University Bonn, Dahlmannstraße 2, 53113 Bonn, Germany
[b] Institute for Medical Microbiology, Immunology and Parasitology, Pharmaceutical Microbiology Unit, Meckenheimer Allee 168, Rheinische Friedrich-Wilhelms-University Bonn, 53115 Bonn, Germany
[c] Biophysical Chemistry, Department of Physical and Theoretical Chemistry, Rheinische Friedrich Wilhelms-University Bonn, Wegelerstraße 12, 53115 Bonn, Germany

ARTICLE INFO

Article history:
Received 24 June 2014
Received in revised form 23 July 2014
Accepted 25 July 2014
Available online 12 August 2014

Keywords:
Molecular dynamics simulation
Lipid II
Nisin
Lipid membrane
Molecular modeling
Antimicrobial peptides

ABSTRACT

Representing a physiological "Achilles' heel", the cell wall precursor lipid II (L_{II}) is a prime target for various classes of antibiotics. Over the years L_{II}-binding agents have been recognized as promising candidates and templates in the search for new antibacterial compounds to complement or replace existing drugs. To elucidate the molecular structural basis underlying L_{II} functional mechanism and to better understand if and how lantibiotic binding alters the molecular behavior of L_{II}, we performed molecular dynamics (MD) simulations of phospholipid membrane-embedded L_{II} in the absence and presence of the L_{II}-binding lantibiotic nisin. In a series of 2×4 independent, unbiased 100 ns MD simulations we sampled the conformational dynamics of nine L_{II} as well as nine L_{II}–nisin complexes embedded in an aqueous 150 mM NaCl/POPC phospholipid membrane environment. We found that nisin binding to L_{II} induces a reduction of L_{II} mobility and flexibility, an outward shift of the L_{II} pentapeptide, an inward movement of the L_{II} disaccharide section, and an overall deeper insertion of the L_{II} tail group into the membrane. The latter effect might indicate an initial step in adopting a stabilizing, scaffold-like structure in the process of nisin-induced membrane leakage. At the same time nisin conformation and L_{II} interaction remain similar to the 1WCO L_{II}–nisin NMR solution structure.

1. Introduction

The discovery, development and clinical exploitation of antibiotics count among the most significant medical advances of the previous century. Reducing the mortality rate from bacterial infections and diseases, antibiotics have become cornerstones of modern medicine required by many common procedures such as transplantation, chemotherapy for cancer or surgery [1]. However, antibiotics lose their efficiency after a period of months to years [2–4], eventually producing new strains of bacteria resistant to the given drug. Since old antibiotics lose their efficiency faster than new ones can be developed [5], there is currently no antibiotic in clinical use, to which resistance has not yet been reported [6,7]. Even in developed countries bacterial infections again count among the top five causes of death, while at the same time the approval rates of new antibiotics have been declining continuously since the 1980s [8,9]. As the need to discover and develop new agents is paramount for modern biomedical research, a detailed understanding of the molecular basis of antibiotics resistance is essential. Discovering and developing new antibiotics can be done designing a drug specifically aiming at a previously identified potential target, e.g. an antibacterial defense mechanism such as multidrug efflux transporters of the resistance nodulation division protein super family [10,11]. Alternatively, an existing antimicrobial compound, that is for example part of an antibacterial attack mechanism, can be optimized to increase its efficiency and band width. For both strategies, however, a detailed understanding of the molecular interactions between drug and target is required.

In bacteria, lipid II (L_{II}) is a central component of the enzymatic cell wall building machinery, translocating the monomeric peptidoglycan units from the cytoplasm to the outside of the membrane. L_{II} consists of a long undecaprenyl (bactoprenol) hydrocarbon chain that is coupled to a monomeric peptidoglycan unit through a pyrophosphate linker. The peptidoglycan unit is the basic building block of the bacterial cell wall and comprises the two amino sugars N-acetylglucosamine (GlcNAc) and N-acetylmuramic acid (MurNAc), with a pentapeptide bound to the latter (Fig. 1a). Due to its function, L_{II} represents a primary molecular target for a large number of antibiotics [12].

Nisin is a lantibiotic produced by numerous strains of lactic acid bacteria. Lantibiotics are antimicrobial peptides comprising intramolecular rings formed by the thioether amino acids lanthionine and

* Corresponding author.
E-mail address: chkandt@mail.de (C. Kandt).

http://dx.doi.org/10.1016/j.bbamem.2014.07.024
0005-2736/

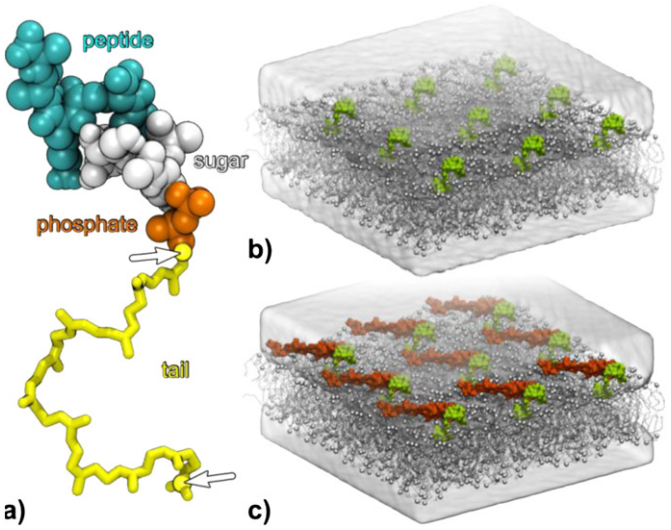

Fig. 1. Lipid II domain structure (a) and simulation starting structures (b, c). To better understand the structural basis underlying the functional mechanism of the cell wall precursor lipid II we computed samples of its dynamics in an aqueous 150 mM NaCl/POPC phospholipid membrane environment in the absence (b) and (c) presence of the lantibiotic nisin. For each system we performed a series of 4 independent, unbiased 100 ns molecular dynamics simulations. The arrows in (a) mark the lipid II atoms used for the tail length vs. membrane insertion depth analysis shown in Fig. 6.

3-methyllanthionine [13,14]. Belonging to the class of type-A lantibiotics, elongated, screw-shaped peptides with a positive net charge, nisin is active against a wide range of Gram-positive bacteria [15,16]. Highly polar, antimicrobial peptides like nisin often form amphipathic structures when interacting with membranes [17,18], and nisin kills bacteria by perforating the cell membrane [19,20], targeting L_{II}. The pyrophosphate of L_{II} was identified as the binding site for nisin, around which two of nisin's lanthionine rings form a cage-like structure [21]. Numerous studies showed that nisin binding to L_{II} results in membrane pore formation [14,22–24], a process in which L_{II} not only acts as mere receptor but is an active constituent of the L_{II}–nisin pore whose stability depends on the length of the L_{II} alkyl chain [25]. Beyond altering the membrane the specific interaction of nisin and L_{II} leads to the inhibition of cell wall biosynthesis, because L_{II} is sequestered and removed from the enzymatic reaction cycle [22]. Notably, when the interaction of nisin with bacterial or artificial membranes was directly observed using fluorescently labeled nisin, the peptides were not homogeneously distributed on the membrane, but rather clustered in large aggregates [23,26]. While this might be explicable in bacterial membranes, it is astonishing that this was also observed for L_{II}-containing model membranes.

To obtain insight into the molecular mechanism, by which nisin – just binding to the pyrophosphate unit of L_{II} – can produce the discussed very diverse effects, we performed MD simulations to understand if and how nisin alters the molecular behavior of membrane-embedded L_{II}. Whereas previous computational studies have focused either on single L_{II} molecules in different bilayer environments [27] or on L_{II} interacting with vancomycin [28,29], here we sampled L_{II} conformational dynamics in two series of four unbiased, independent 100 ns MD simulations of nine L_{II} as well as nine L_{II}–nisin complexes embedded in a POPC membrane in physiological salt solution. We find that nisin alters L_{II} membrane insertion inducing (i) longer prenyl tail conformations intruding deeper into the membrane; (ii) an outwards shift of the L_{II} pentapeptide section while (iii) the disaccharide section inserts deeper into the membrane. In addition, complexation with nisin lowers the L_{II} diffusion speed as well as the overall volume occupied by L_{II}. At the same time the nisin conformation and key residues of L_{II} interaction remained similar to the known 1WCO L_{II}–nisin NMR solution structure [21].

2. Materials and methods

2.1. Simulation details

MD simulations were performed employing *GROMACS* version 4.0.3 [30,31] and the GROMOS96 force field with the 54a7 parameter set [32]. In all simulations standard protonation states were assumed for titratable residues and all bond lengths were constrained by LINCS [33] so that an integration time step of 2 fs could be chosen. Systems were simulated at 300 K, maintained separately for protein, lipids and water + ions by a Berendsen thermostat [34] with a time constant (τ_T) of 0.1 ps. Pressure coupling was done employing a Berendsen barostat [34] using a 1 bar reference pressure and a time constant of 4 ps. To permit bilayer fluctuations in the membrane plane semiisotropic pressure coupling was used. Electrostatic interactions were calculated using particle mesh Ewald (PME) Summation [35,36], and twin range cutoffs of 1.0 and 1.4 nm were applied for computing the van der Waals interactions.

Starting point for all simulations was conformer 1 of the 1WCO L_{II}–nisin NMR solution structure [21] after completing the truncated 3LII variant using the full length L_{II} structural model (Fig. 1a) by Jia and co-workers [28], from which we also adapted the simulation parameters. Details on the nisin simulation parameters can be found in the supplemental material and supplemental Fig. 1. Simulation systems were constructed inserting a single L_{II}–nisin or L_{II}, respectively, into a pre-equilibrated 128 lipid POPC bilayer patch [37] using *InflateGRO2* [38]. In this process 2 POPC lipids were deleted from the L_{II}-containing leaflet. Next, each simulation system was extended three times in X and Y direction using GROMACS tool *genconf* and subsequently solvated in an aqueous 150 mM NaCl solution yielding a total charge of 0. The final simulation systems comprise 9 L_{II}; 1134 POPC; 5,9150 H_2O; 335 Na^+ and 308 Cl^- at a total system size of 238,357 atoms (Fig. 1b) as well as 9 L_{II}–nisin; 1134 POPC; 57,787 H_2O; 308 Na^+ and 310 Cl^- at a total system size of 236,799 atoms (Fig. 1c). Following steepest descent energy minimization and 0.5 ns equilibration at constant volume and temperature, four independent, unbiased 100 ns MD runs were initiated for each simulation system using different random seed numbers in generating the starting velocities.

2.2. Analysis

Using the GROMACS tool *g_density* [30,31] we computed 1-dimensional density profiles to determine the overall distribution of the system components. After least-square fitting on the POPC phosphorous atoms partial densities were computed for the POPC bilayer, L_{II}, its structural domains and nisin using the last 50 ns of the trajectories. To gain further insight into L_{II}-interaction with the membrane and nisin, we computed the average amount of ≤4 Å heavy atom contacts between L_{II}'s four structural domains (peptide section, dissacharide, phosphate and hydrophobic tail) and the POPC head and tail groups as well as nisin. The analysis was performed on the last 50 ns of the trajectories using the GROMACS tool *g_mindist* [30,31] as well as *xmgrace* for averaging and visualization.

In order to elucidate whether nisin alters the conformational dynamics of L_{II}'s hydrophobic tail, we computed for all trajectories the distance between the first and last atom of the L_{II}-tail (Fig. 1a) as well as monitored the Z coordinate of the LII-tail tip atom. Computed over the last 50 ns, the analysis was performed for all trajectories calculating and plotting the resulting tail length vs. insertion depth distributions in *QtiPLOT*.

Assessing the amount of space occupied by L_{II}, its structural domains and nisin, each trajectory was converted to a voxel-based representation of spatial density, for which profiles of cross-sectional area along the membrane normal were computed. Following the initial least square alignment of the POPC phosphorus atoms, the last 50 ns of each of the 36 L_{II} and L_{II}–nisin molecules were aligned using lateral translations

within the membrane plane. Subsequently, each individual L_{II}/L_{II}–nisin trajectory was converted into spatial densities via the *VMD 1.9.1* plugin VolMAP [39] using a resolution of 1 $Å^3$. Using dxTuber [40], spatial densities exceeding 0.01 atoms $Å^{-3}$ were processed to extract the cross-sectional area profiles along the membrane normal subsequently averaged and plotted using *QtiPLOT*.

Using the L_{II} phosphate group as a reference we computed L_{II} lateral diffusion coefficients (LDC) in the presence and absence of nisin to assess whether nisin binding affects L_{II} diffusion speed. Using the GROMACS tool g_msd the analysis was carried out for each L_{II} molecule individually and subsequently averaged for the L_{II} and L_{II}–nisin simulation scenarios. As linear sections of the mean square displacement graphs suitable for LDC calculation time windows of 40–60 ns and 30–50 ns were used for the L_{II} and L_{II}–nisin runs respectively.

Aiming at quantifying nisin conformational changes and L_{II} interaction and comparing our L_{II}–nisin model to experimental data, we computed nisin α-carbon root mean square displacements (Cα-RMSDs) after least square fitting to the starting conformation of each nisin molecule and calculated mean smallest distances between the heavy atoms of each nisin residue and L_{II} structural components using the GROMACS tool *mdmat*. Carried out over the last 25 ns simulation time the analysis was averaged over all L_{II}–nisin simulations. For comparison, we computed both pair-wise Cα-RMSDs and per-residue mean smallest distances for all 20 conformers of the NMR L_{II}–nisin solution structure [21]. For this analysis the time window of the last 25 ns was chosen as only after 75 ns the increase of nisin Cα-RMSD has slowed down in all of the 4 × 9 cases considered.

Using the GroMACS tool *g_mindist*, we monitored over time the amount of ≤0.4 nm heavy atom contacts between nisin and the POPC tail groups to analyze nisin–membrane interaction and insertion. Moreover, we employed the GroMACS tool *g_traj* to determine for each nisin residue the minimum heavy atom Z-position after prior translational least square fitting of the trajectories on the POPC phosphorous atoms in the starting structure. Averaged over all 36 nisin molecules in all 4 simulations the analysis yields nisin's per residue membrane insertion depth as a function of time which we visualized using *QtiPLOT*.

3. Results

3.1. Nisin conformational changes and model validation

To determine the amount of nisin conformational changes we computed Cα RMSDs after least square fitting to the starting structure (Fig. 2a). While the RMSD increase has slowed down in all simulations after 75 ns, we do not observe stable RMSD plateaus for the 4 × 9 nisin molecules with RMSDs ranging from 0.33 nm up to 0.88 nm after 100 ns simulation time. Snapshots of simulation end conformations are given in the Supplemental Figs. 2 and 3. However, compared to the L_{II}–nisin NMR solution structure [21] in our MD simulations the range of conformational differences to the starting structure is smaller than within the conformational ensemble of the NMR structure exhibiting pair-wise Cα-RMSDs up to 1.1 nm (Fig. 1a, inset). This means that the amount of conformational space nisin samples throughout our simulations lies well within the range of conformational diversity observed experimentally for nisin complexed with the truncated 3 isoprenoid unit LII variant [21].

To obtain more detailed structural information on the validity of the simulation results, we computed per-residue mean smallest distances of lipid II and nisin (Fig. 2b). Taking into account all non-hydrogen atoms and computed for the last 25 ns of all L_{II}–nisin simulations (Fig. 2b, lower half), the analysis was also performed on the conformational ensemble of the L_{II}–nisin NMR structure. The numbering scheme used for the residues is illustrated in Fig. 2c. Comparing MD simulation and experimental data we find that the mean smallest distances matrices are very similar, including the residues directly involved in close-range L_{II}–nisin interactions. This finding further speaks in favor of the validity of the MD simulations.

3.2. Partial densities

Next, we calculated partial density profiles along the membrane normal for the POPC bilayer, L_{II} and its structural domains as well as for nisin (Fig. 3). The profiles were averaged over the last 50 ns of the simulations. Both without (Fig. 3a and b) and with nisin (Fig. 3c and d), the POPC membrane displays similar density profiles ranging from −3.2 to 3.2 nm (bilayer center at 0 nm) with POPC head group maxima at −2 and 2 nm. In both scenarios the L_{II}/ L_{II}–nisin containing leaflet exhibits a slightly lowered maximum due to the lipids removed on this side to accommodate L_{II}. Zooming in on the L_{II} density (Fig. 3b), we find L_{II} displaying a double peak profile extending from outside the membrane at 3.6 nm over to the opposite leaflet at −1.6 nm with density maxima at 0.4 nm and 2.2 nm. Whereas the maximum within the membrane stems from the L_{II}-tail section, the maximum at the membrane surface results from the L_{II}-phosphorus (maximum at 2.2 nm), L_{II}-sugar (maximum at 2.6 nm) and L_{II}-peptide sections (maximum at 2.4 nm). In the L_{II}–nisin simulations the L_{II} profile again features two peaks. However, whereas the L_{II} head group is still located at the membrane surface (maximum at 2.4 nm), the L_{II}-tail

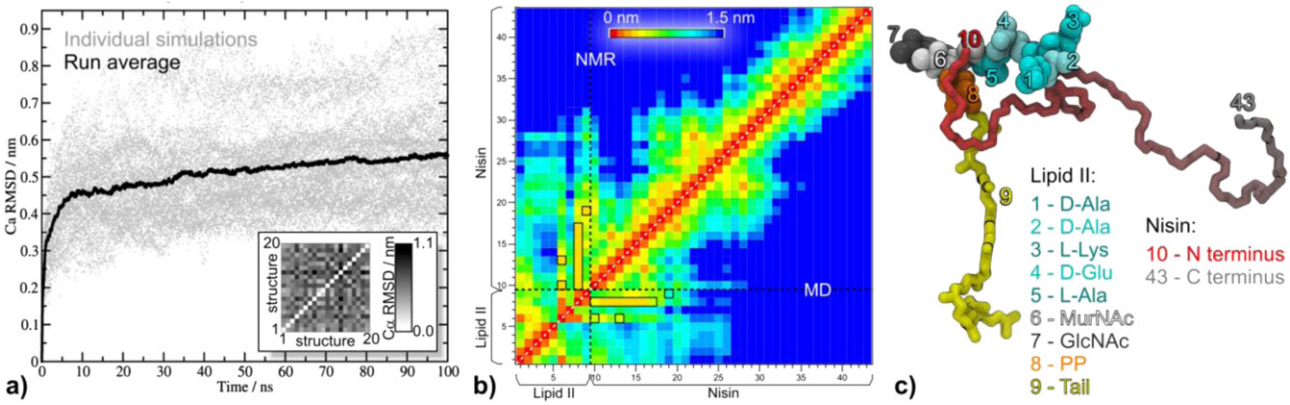

Fig. 2. Conformational changes and comparison to the 1WCO 3L_{II}–nisin NMR solution structure. Nisin conformational drift was determined computing Cα root mean square displacements (RMSDs) after least square fitting to the starting structure (a). As illustrated by the inset in the same panel, after 100 ns the conformational differences to the simulation starting structure smaller than within the ensemble of the NMR solution structure. For a more detailed comparison between simulation and experiment we computed the mean smallest distances between the heavy atoms of L_{II}/nisin residues for the 1WCO NMR structure (b, upper half) and the last 25 ns of all L_{II}/nisin simulations (b, lower half). For clarity residues forming the L_{II}/nisin interface in the 1WCO NMR structure are marked by a black outline. The residue numbering scheme employed is illustrated in (c) using a L_{II}/nisin simulation end conformation as an example.

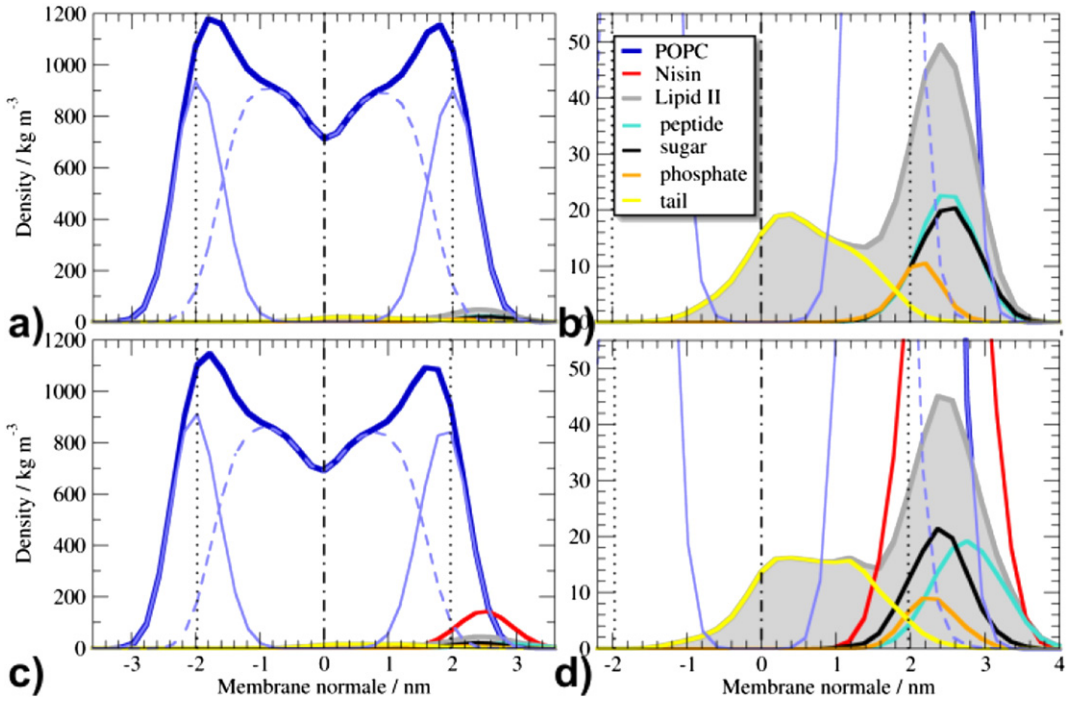

Fig. 3. Partial density profiles along the membrane normal computed for the POPC bilayer, L_{II} and its structural domains as well as nisin averaged over the last 50 ns of the simulations. Whereas (a, b) depict the results for the L_{II} simulations in absence of nisin, (c, d) show the outcome for L_{II} complexed with nisin. (b, d) show magnified views focusing on L_{II} and its structural domains. The bilayer center is shifted to zero and highlighted by a dashed vertical line, and maxima of the POPC head group density are indicated by vertical dotted lines.

density now displays a plateau ranging from 0.2 nm to 1.2 nm. Furthermore, the L_{II}-sugar density is shifted inwards (maximum at 2.2 nm), while the L_{II}-peptide density is shifted outwards (maximum at 2.8 nm) extending 0.8 nm out of the membrane. Ranging from 1.2 to 3.8 nm, the nisin density peaks at 2.6 nm.

3.3. Volume occupied by lipid II and nisin

To quantify the amount of space accessed by L_{II}, its structural domains, and nisin we computed mass-weighted spatial densities based on the last 50 ns of the simulations. Shown as averaged profiles of cross-sectional area (CSA) along the membrane normal, the outcome of these analyses is plotted in Fig. 4. Without nisin the overall shape of L_{II}'s CSA profile approximates a combination of two Gaussians with different amplitudes displaying a first maximum at 0.3 nm due to the L_{II}-tail and a second maximum at 2.6 nm stemming from the L_{II}-peptide, -sugar and -phosphate sections peaking at 2.7 nm and 2.3 nm, respectively (Fig. 4a). When nisin is bound, the overall shape of the L_{II} CSA profile remains the same, but the distribution is more compact and stretched out (Fig. 4b, c). Whereas the CSA profile of the L_{II}-phosphate section is unchanged, the ones of the L_{II}-sugar and -tail sections are shifted towards the bilayer center and the L_{II}-peptide CSA is broadened in particular towards the water phase (Fig. 4b). Ranging from the water phase to halfway between POPC head group maximum density and bilayer center, nisin accesses a maximum CSA of 900 Å^2 at 2.4 nm (Fig. 4c).

3.4. Lipid II lateral diffusion speed

To assess whether complexation with nisin alters L_{II}'s lateral diffusion speed we computed lateral diffusion coefficients (LDC) in the absence and presence of nisin using the L_{II} phosphate group as reference. Computed and subsequently averaged for all L_{II} molecules in the two simulation scenarios we find LDCs of 23.7 ± 9.3 μm^2/s for the L_{II} runs and 14.5 ± 6.5 μm^2/s for the L_{II}–nisin simulations, suggesting that complexation with nisin lowers the L_{II} diffusion speed.

3.5. Lipid II close range interactions

To characterize L_{II}'s close range interactions with the POPC membrane and with nisin, we determined the amount of contacts with distances smaller or equal than 0.4 nm between the various L_{II} structural domains and the lipid head and tail groups as well as nisin. Run- and time-averaged over the last 50 ns of the L_{II} and L_{II}–nisin trajectories the results of the analysis are shown as bar diagrams in Fig. 5.

Whereas in the L_{II} simulations close contacts occur predominantly between POPC head groups and the L_{II}-peptide and L_{II}-sugar sections, followed by L_{II}-phosphate and L_{II}-tail section, in the L_{II}–nisin simulations interactions with the POPC head groups occur mainly via the L_{II}-sugar section followed by the L_{II}-peptide, L_{II}-tail and L_{II}-phosphate section (Fig. 5, left). Close contacts with the POPC tail groups predominantly involve of course the L_{II}-tail section, followed by the L_{II}-peptide, L_{II}-sugar and L_{II}-phosphate sections in the L_{II}-simulations, whereas in the L_{II}–nisin runs POPC tail group interaction is dominated by the L_{II}-tail and L_{II}-sugar sections followed by the L_{II}-peptide and L_{II}-phosphate sections (Fig. 5, middle). In agreement with experimental data [21] L_{II}–nisin close range interactions mainly involve the L_{II}-phosphate section followed by the L_{II}-peptide, L_{II}-sugar and L_{II}-tail sections (Fig. 5c, right).

3.6. Lipid II tail length and insertion depth

Nisin is known to induce pores in L_{II}-containing membranes [14, 22–24]. To understand if and how nisin changes L_{II} conformation and dynamics in this context we analyzed the extension of the L_{II} tail, and how deep its tip (see arrows in Fig. 1a) intrudes into the bilayer in the absence and presence of nisin. Computed and averaged of over the last 50 ns of the simulations the resulting distributions are shown in Fig. 6.

Focusing on regions of coherent mid-range occupancy of 50 or more conformations, the resulting distribution of the L_{II} runs ranges from 1.1 nm tail length and an insertion depth of 1.6 nm to a tail length of

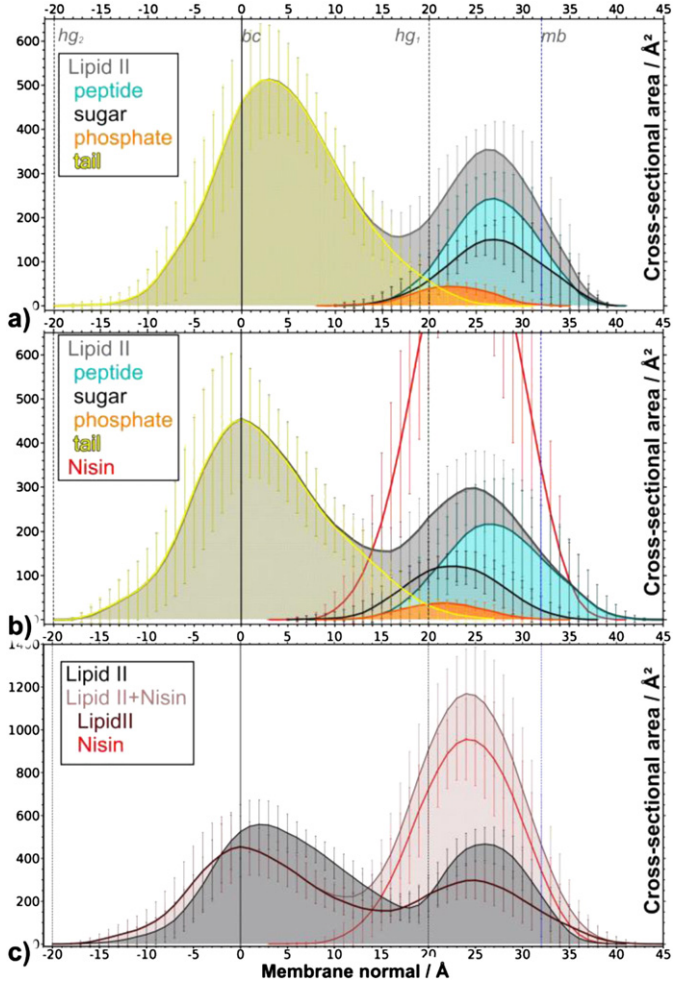

Fig. 4. Profiles of cross-sectional area through the overall volume accessed by L_{II}, its structural domains and nisin throughout the last 50 ns of the simulations. Whereas (a) depicts the results for the L_{II} simulations, panel (b, c) show our findings for the L_{II}–nisin runs. Panel (c) provides an overview of the volumes occupied by L_{II}, nisin and by the L_{II}–nisin complex. The profiles shown are time and run averages calculated over all 4×9 L_{II} and nisin molecules with the error bars representing standard deviations. For clarity vertical lines have been added representing the bilayer center (bc), the maxima of POPC head group density in both leaflets (hg_1, hg_2) as well the beginning of POPC density (mb) marking the first leaflet's border towards the water phase.

3.5 nm and an insertion depth of −1.0 nm extending well into the opposite bilayer leaflet. Maximal occupancies occur at a tail length of 2.4 nm and a tip position at the bilayer center (0 nm) as well as at a length of 3.1 nm and an insertion depth of −0.8 nm (Fig. 6a). As shown in Fig. 6b the presence of nisin clearly changes the L_{II} tail behavior resulting in longer L_{II}-tail lengths and a deeper membrane insertion as maximum occupancies occur at tail lengths of 2.3 nm extending into the bilayer center (0.0 nm), at tail lengths of 3.1 nm inserting to −1 nm and even at tail lengths of 3.5 nm inserting to down to −1.3 nm.

3.7. Nisin membrane insertion

In order to further assess nisin–membrane interaction as well as check for trends of beginning pore formation or membrane distortion, we analyzed nisin's membrane insertion as a function of simulation time (Fig. 7). To this end, we monitored the number of contacts between the heavy atoms of nisin and the POPC tail groups within a distance cutoff of ≤0.4 nm. We find the number of contacts increasing by a factor of 3–4 throughout the simulations (Fig. 7a) suggesting an increasing insertion of nisin into the bilayer. To obtain detailed information, which residues were preferentially involved, we computed for each nisin residue in each simulation its minimum heavy atom Z-position as a function of time (see Supplemental Fig. 4). To summarize the complex information of that graphs, we subsequently averaged over all 9 individual nisins in the 4 MD runs (Fi. 7b). We find the deepest membrane insertion occurring at Leu6 and Dha5 inside the A-ring as well as Pro9 in the B-ring, displaying respective average minimum Z positions of 1.5–1.45 nm, 1.6 nm and 1.7 nm. Continuously displaying average Z-positions above 2.6 nm, Gly18 in the C-ring exhibits the shallowest membrane insertion. Generally, rings A and B intrude deepest into the membrane, followed by the D and E rings as well as the C-terminus, whereas N-terminus and ring C show the least insertion. While we observe a deepening of membrane insertion in the C-ring, the N-terminus, Lys12 or Asn20, nisin's overall average insertion depth stays constant throughout the simulated 100 ns time scale. No trends of beginning pore formation were detected.

4. Discussion

Although a prime target of different classes of antibiotics little is known about L_{II} structure and dynamics and how these are affected by lantibiotics targeting L_{II}. Addressing the question if and how nisin binding alters the behavior of membrane-embedded L_{II}, we report the first simulation study investigating this topic in two series of four independent, unbiased 100 ns MD simulations each comprising nine L_{II} and L_{II}–nisin molecules embedded in a POPC lipid bilayer. With nisin conformational dynamics and L_{II} interaction similar to the 1WCO $3L_{II}$–nisin NMR solution structure, we find that nisin alters L_{II} membrane insertion, L_{II} interaction with the POPC head and tail groups, as well as the overall volume accessed by L_{II}. We begin this section discussing the limitations and caveats of our approach and then proceed to our findings and their biological implications.

4.1. Limitations of our approach

Whereas the lipid composition of Gram-positive bacteria is highly diverse varying greatly from species to species [41], in this study we employed a homogeneous POPC bilayer as model membrane. While certainly different from the in vivo conditions we nevertheless consider our simplified membrane environment a reasonable starting point to study L_{II} dynamics for two reasons. Firstly, fluorescence microscopy experiments indicated similar L_{II}–nisin diffusion and aggregation behavior in POPC membranes as in DOPC/DOPG bilayers [23]. Secondly, as one of the most widely used lipid models for MD simulations [42–51], simulation parameters for POPC and other lipids comprising phosphatidylcholine (PC) head groups count among the most reliable currently available [37,52–56]. Moreover POPC has been successfully employed in earlier MD studies yielding biologically meaningful insights, even for cases where the native lipid environment does not comprise POPC [28,49–51,57].

As high resolution 3D structural data for L_{II} are scarce, computational models can provide valuable insights into the molecule's conformational and dynamical properties. Whereas previous simulation studies investigated single or dual L_{II} molecules [27] or single L_{II} in conjunction with vancomycin [28,29], here we focus on how L_{II} and nisin interact and how the lantibiotic changes the molecular behavior of L_{II}.

For any MD study the gained insights depend on the quality of the computational model used and the amount of conformational sampling achieved. Representing the first MD study investigating L_{II}–nisin interaction, we adopted the L_{II} simulation parameters from [28] while developing our own for nisin (supplemental material, supplemental Fig. 1). Considering the obtained similarity of simulation and experiment in terms of overall conformational variety (Fig. 2a) and nisin–L_{II} interaction (Figs. 2b, 5 right), we consider our L_{II}–nisin model a reasonable starting point for gaining insights into the cytotoxic effects of nisin.

Whether the amount of conformational sampling in an MD simulation study is sufficient depends on the respective questions the study

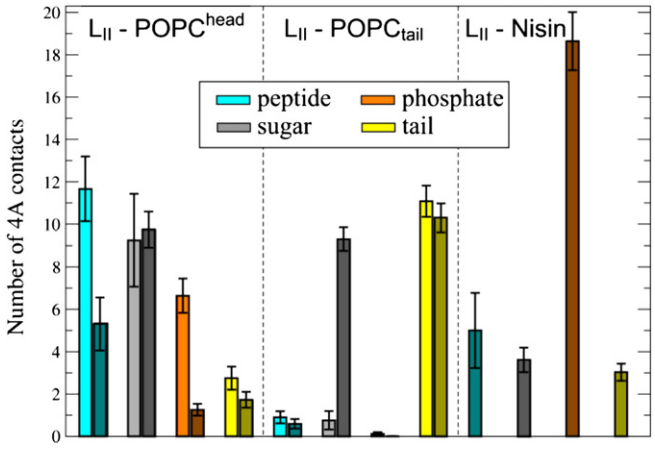

Fig. 5. Close range interactions between L_{II}'s structural domains and POPC head (left) and tail groups (middle) as well as nisin (right). The bar diagrams illustrate the amount of short distance interactions (≤4 Å) averaged over the last 50 ns of the simulations with error bars indicating standard deviations. Whereas the findings from the L_{II} simulations are shown in bright colors, dark tones represent the results for the L_{II}–nisin runs.

seeks to answer. In this study we addressed the question if nisin alters the molecular behavior of L_{II} in a multi-copy MD approach [58–65] yielding a total of $4 \times 9 \times 100$ ns dynamics samples for both L_{II} and L_{II}–nisin. Whereas that amount of sampling was expectedly not long enough to observe nisin-induced pore formation (Fig. 7), with L_{II} membrane insertion (Figs. 3, 6), L_{II}–phospholipid interaction (Fig. 5) and L_{II} volume occupied (Fig. 4) we identified three L_{II} properties altered by nisin whose functional implications we discuss below. Against that background we consider the amount of conformational sampling adequate to the question we sought to answer.

4.2. Functional implications

Beyond acting as a landing platform form for nisin [27], L_{II} plays a key role in nisin's cytotoxic effect of cell wall synthesis inhibition and membrane perforation [14,22,23,25]; a process to which the length of the L_{II} prenyl tail [25] and the nisin binding-induced aggregation of L_{II} is also of great importance [23,26]. Focusing on L_{II} structure and behavior we find that in a phospholipid environment nisin clearly changes L_{II}'s molecular behavior on a 100 ns time scale.

Whereas at first glance the partial density profiles (Fig. 3) suggest that L_{II}'s overall incorporation into the membrane changes little upon

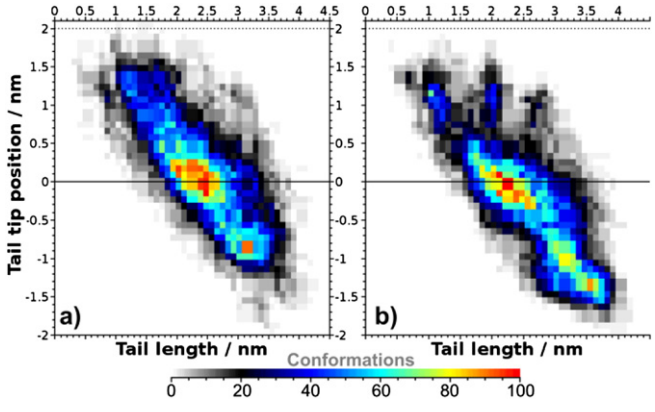

Fig. 6. L_{II} tail tip insertion depth versus L_{II} tail length distribution computed over the last 50 ns of the L_{II} simulations (a) and the L_{II}–nisin runs (b). For clarity horizontal lines indicate the center of the bilayer at 0 nm and the maximum of POPC head groups density at 2 nm. Nisin binding to L_{II} shifts the distribution favoring more extended tail conformations intruding further into the membrane.

nisin binding, inspecting how the individual L_{II} structural domains contribute to the overall profile reveals distinct changes. The prenyl tail distribution is more smeared out, so that it is distributed more evenly between membrane head group region and the opposite monolayer while extending slightly deeper into the membrane (Fig. 3 b, d). Moreover, the pentapeptide now resides slightly more outside the lipid head group region, probably due to steric hindrance effects and interaction with nisin. At the same time the disaccharide moiety has shifted deeper into the membrane as additionally indicated by the increased amount of close contact interactions to the POPC tail groups (Fig. 5) as well as the cross-sectional area (CSA) profiles through the volume occupied by L_{II} and L_{II}–nisin (Fig. 4). Taken together these observations can be interpreted as suggesting a two-level mechanism by which nisin inhibits cell wall synthesis: Sterically hindering access to the L_{II}-phosphate and pentapeptide section through direct interaction, nisin additionally pushes the cleavage site of the peptidoglycan building block deeper into the membrane and thus out of reach for enzymatic access.

Furthermore, the CSA analyses also indicated the increasing amount of molecular material in the POPC head group region, where the L_{II}–nisin complex occupies an area that is 2.4 times larger than L_{II} alone. This finding implies that e.g. the lateral mobility of the L_{II}–nisin complex within the membrane should clearly be reduced in comparison to unbound L_{II} which could recently be confirmed experimentally [66] and is also in agreement with our findings of lower lateral diffusion coefficients in the L_{II}–nisin simulations. Moreover, one could hypothesize that on longer time scales the increased molecular diameter would modify membrane curvature and exert a certain stress on the bilayer producing a trend to vesicle budding. Potential ways to test this hypothesis could include multi scale simulations like in [67–69], comparing the microsecond behavior of larger L_{II}/L_{II}–nisin systems as well as combined fluorescence/ microscopy experiments similar to the ones carried out in [66].

Comparing the L_{II} prenyl tail dynamics with and without nisin, we found that its CSA profile is reduced in the complex, while simultaneously extending deeper into the membrane (Fig. 4c), indicating a decreased flexibility accessing less space. Further evidence of nisin influencing the L_{II} prenyl tail was seen when we evaluated the extension of the L_{II} prenyl tail and its maximum insertion depth into the membrane (Fig. 6.). Clearly, nisin-binding to L_{II} results in more extended prenyl tail conformations intruding deeper into the membrane, now almost reaching the maximum density of the lipid head groups on the opposite face of the membrane. If our simulations are correct our findings can provide a structural explanation why a stable L_{II}–nisin pore complex requires a minimum length of the prenyl tail as demonstrated by Breukink and co-workers [25]: in reaching far over to the opposite leaflet the prenyl tail fulfills a stabilizing function, enabling L_{II} to adopt a scaffold-like structure along which the pore complex with nisin is formed. Possible scenarios to test this hypothesis experimentally could include marking the L_{II} tail tip as well the inner leaflet's headgroups e.g. by fluorescence labels exhibiting Förster resonance energy transfer. Increased fluorescence in the presence of nisin would then argue for our hypothesis of L_{II} stretching out and nearly spanning the entire membrane in the presence of nisin. If our simulations are correct our data support the hypothesis that L_{II} is not only a passive binding site for nisin but also an active player in the cytotoxic process whose molecular behavior is altered once nisin is bound.

Taken together, our in silico observations discussed above are well compatible with the experimentally confirmed effect of nisin inducing membrane perforations [14,22,24,25] and vesicle budding [23,66] in L_{II} containing membranes. So far, our simulations do not allow drawing conclusions about the nature of the nisin-induced L_{II} aggregation. Obviously, this phenomenon occurs on a different time-scale than the dynamics that we examined in this study. To observe directly L_{II} aggregation and pore formation, the simulation duration must substantially be prolonged, underscoring the need for long-time simulations using both atomistic [70] and coarse-grained approaches [71–73].

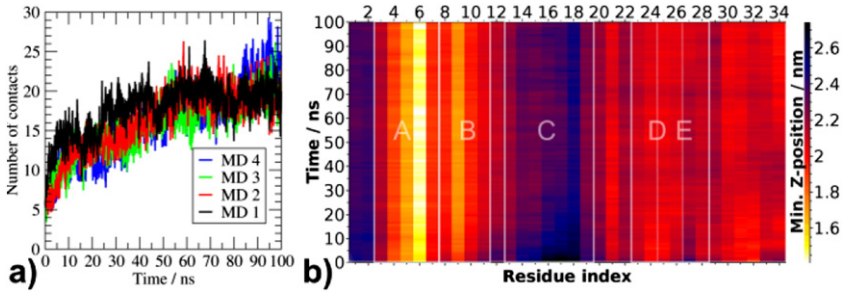

Fig. 7. Close range interactions between nisin and the lipid bilayer. (a) Number of contacts ≤4 Å between the peptide's heavy atoms and the POPC tail groups as a function of time; (b) average insertion depth per residue expressed as minimum Z-position of the peptide's non-hydrogen atoms with the color code defined at the right hand side. As above, the bilayer center is located at z = 0 nm, and the maximum of the POPC head group density is at 2 nm. For clarity, vertical lines indicate nisin's five intramolecular rings A–E.

5. Conclusions

Addressing the question if and how complexation with nisin alters the molecular behavior of L_{II} in a phospholipid environment we carried out molecular dynamics simulations of L_{II} with and without nisin. On a 100 ns time scale we find that nisin alters L_{II} behavior inducing an outward shift of the L_{II} pentapeptide and an inward movement of the L_{II} disaccharide section, suggesting that nisin binding not only sterically hinders access to L_{II} but also pushes the cleavage site of the peptidoglycan building block out of enzymatic reach pushing it deeper into the membrane. Moreover we find a reduction in L_{II} mobility and flexibility that is in line with recent experimental evidence as well as a deeper insertion of the L_{II} prenyl tail which might play a stabilizing function in the process of nisin-induced membrane leakage.

Acknowledgments

This work was financially supported by the Ministerium für Innovation, Wissenschaft und Forschung des Landes Nordrhein-Westfalen and the Deutsche Forschungsgemeinschaft. ChK is a junior research group leader funded by the NRW Rückkehrerprogramm. HGS acknowledges support by the Bonfor program of the Medical Faculty of the University of Bonn. We gratefully acknowledge constructive discussions of the presented results with Prof. Dr. Heike Brötz-Oesterhelt and Katharina Scherer.

Appendix A. Supplementary data

Supplementary data to this article can be found online at http://dx.doi.org/10.1016/j.bbamem.2014.07.024.

References

[1] WorldHealthOrganization, WHO | Antimicrobial Resistance, Fact Sheet °194, 2012.
[2] R. Cohen, Approaches to reduce antibiotic resistance in the community, Pediatr. Infect. Dis. J. 25 (2006) 977–980.
[3] T.J. Dougherty, J.F. Barrett, M.J. Pucci, Microbial genomics and novel antibiotic discovery: new technology to search for new drugs, Curr. Pharm. Design. 8 (2002) 1119–1135.
[4] D. McDevitt, M. Rosenberg, Exploiting genomics to discover new antibiotics, Trends Microbiol. 9 (2001) 611–617.
[5] R.G. Wax, K. Lewis, A.A. Salyers, H. Taber, Bacterial Resitance to Antimicrobials, 2CRC Press, Taylor & Francis Group, LLC, Boca Raton, 2008.
[6] E. Breukink, B. de Kruijff, Lipid II as a target for antibiotics, Nat. Rev. Drug Discov. 5 (2006) 321–332.
[7] H. Nikaido, Multidrug resistance in bacteria, Annu. Rev. Biochem. 78 (2009) 119–146.
[8] J.E. Bandow, N. Metzler-Nolte, New ways of killing the beast: prospects for inorganic–organic hybrid nanomaterials as antibacterial agents, Chembiochem 10 (2009) 2847–2850.
[9] M. Wenzel, B. Kohl, D. Munch, N. Raatschen, H.B. Albada, L. Hamoen, N. Metzler-Nolte, H.G. Sahl, J.E. Bandow, Proteomic response of *Bacillus subtilis* to lantibiotics reflects differences in interaction with the cytoplasmic membrane, Antimicrob. Agents Chemother. 56 (2012) 5749–5757.
[10] H. Nikaido, Structure and mechanism of RND-type multidrug efflux pumps, Adv. Enzymol. Relat. Areas Mol. Biol. 77 (2011) 1–60.
[11] A.V. Vargiu, F. Collu, N. Fischer, C. Kandt, Molecular dynamics computer simulations of multidrug RND P. Ruggerone efflux pumps, Comput. Struct. Biotechnol. J. 5 (2013) (e2013302008).
[12] T. Schneider, H.G. Sahl, An oldie but a goodie — cell wall biosynthesis as antibiotic target pathway, Int. J. Med. Microbiol. 300 (2010) 161–169.
[13] E. Gross, J.L. Morell, The structure of nisin, J. Am. Chem. Soc. 93 (1971) 4634–4635.
[14] H. Brotz, M. Josten, I. Wiedemann, U. Schneider, F. Gotz, G. Bierbaum, H.G. Sahl, Role of lipid-bound peptidoglycan precursors in the formation of pores by nisin, epidermin and other lantibiotics, Mol. Microbiol. 30 (1998) 317–327.
[15] A.T.R. Mattick, A. Hirsch, Further observations on an inhibitory substance (Nisin) from lactic streptococci, Lancet 253 (1947) 5–8.
[16] M.K. Rayman, B. Aris, A. Hurst, Nisin: a possible alternative or adjunct to nitrite in the preservation of meats, Appl. Environ. Microbiol. 41 (1981) 375–380.
[17] P.M. Hwang, H.J. Vogel, Structure–function relationships of antimicrobial peptides, Biochem. Cell Biol. 76 (1998) 235–246.
[18] E. Matyus, C. Kandt, D.P. Tieleman, Computer simulation of antimicrobial peptides, Curr. Med. Chem. 14 (2007) 2789–2798.
[19] E. Ruhr, H.G. Sahl, Mode of action of the peptide antibiotic nisin and influence on the membrane potential of whole cells and on cytoplasmic and artificial membrane vesicles, Antimicrob. Agents Chemother. 27 (1985) 841–845.
[20] A. Lamsa, W.T. Liu, P.C. Dorrestein, K. Pogliano, The *Bacillus subtilis* cannibalism toxin SDP collapses the proton motive force and induces autolysis, Mol. Microbiol. 84 (2012) 486–500.
[21] S.T. Hsu, E. Breukink, E. Tischenko, M.A. Lutters, B. de Kruijff, R. Kaptein, A.M. Bonvin, N.A. van Nuland, The nisin–lipid II complex reveals a pyrophosphate cage that provides a blueprint for novel antibiotics, Nat. Struct. Mol. Biol. 11 (2004) 963–967.
[22] I. Wiedemann, E. Breukink, C. van Kraaij, O.P. Kuipers, G. Bierbaum, B. de Kruijff, H.G. Sahl, Specific binding of nisin to the peptidoglycan precursor lipid II combines pore formation and inhibition of cell wall biosynthesis for potent antibiotic activity, J. Biol. Chem. 276 (2001) 1772–1779.
[23] K. Scherer, I. Wiedemann, C. Ciobanasu, H.G. Sahl, U. Kubitscheck, Aggregates of nisin with various bactoprenol-containing cell wall precursors differ in size and membrane permeation capacity, Biochim. Biophys. Acta 1828 (2013) 2628–2636.
[24] I. Wiedemann, R. Benz, H.G. Sahl, Lipid II-mediated pore formation by the peptide antibiotic nisin: a black lipid membrane study, J. Bacteriol. 186 (2004) 3259–3261.
[25] E. Breukink, H.E. van Heusden, P.J. Vollmerhaus, E. Swiezewska, L. Brunner, S. Walker, A.J. Heck, B. de Kruijff, Lipid II is an intrinsic component of the pore induced by nisin in bacterial membranes, J. Biol. Chem. 278 (2003) 19898–19903.
[26] H.E. Hasper, N.E. Kramer, J.L. Smith, J.D. Hillman, C. Zachariah, O.P. Kuipers, B. de Kruijff, E. Breukink, An alternative bactericidal mechanism of action for lantibiotic peptides that target lipid II, Science 313 (2006) 1636–1637.
[27] A. Chugunov, D. Pyrkova, D. Nolde, A. Polyansky, V. Pentkovsky, R. Efremov, Lipid-II forms potential "landing terrain" for lantibiotics in simulated bacterial membrane, Sci. Rep. 3 (2013) 1678.
[28] Z. Jia, M.L. O'Mara, J. Zuegg, M.A. Cooper, A.E. Mark, The effect of environment on the recognition and binding of vancomycin to native and resistant forms of lipid II, Biophys. J. 101 (2011) 2684–2692.
[29] Z. Jia, M.L. O'Mara, J. Zuegg, M.A. Cooper, A.E. Mark, Vancomycin: ligand recognition, dimerization and super-complex formation, FEBS J. 280 (2013) 1294–1307.
[30] H.J.C. Berendsen, D. van der Spoel, R. van Drunen, GROMACS: a message-passing parallel molecular dynamics implementation, Comput. Phys. Commun. 91 (1995) 43–56.
[31] B. Hess, C. Kutzner, D. van der Spoel, E. Lindahl, GROMACS 4: algorithms for highly efficient, J. Chem. Theory Comput. 4 (2008) 435–447.
[32] N. Schmid, A.P. Eichenberger, A. Choutko, S. Riniker, M. Winger, A.E. Mark, W.F. van Gunsteren, Definition and testing of the GROMOS force-field versions 54A7 and 54B7, Eur. Biophys. J. 40 (2011) 843–856.
[33] B. Hess, H. Bekker, H.J.C. Berendsen, J.G.E.M. Fraaije, LINCS: a linear constraint solver for molecular simulations, J. Comput. Chem. 18 (1997) 1463–1472.
[34] H.J.C. Berendsen, J.P.M. Postma, W.F. van Gunsteren, A. DiNola, J.R. Haak, Molecular dynamics with coupling to an external bath, J. Chem. Phys. 81 (1984) 3684–3690.
[35] T. Darden, D. York, L. Pedersen, Particle mesh Ewald— an N. Log(N) method for Ewald sums in large systems, J. Chem. Phys. 98 (1993) 10089–10092.
[36] U. Essmann, L. Perera, M.L. Berkowitz, T. Darden, H. Lee, L.G. Pedersen, A smooth particle mesh Ewald method, J. Chem. Phys. 103 (1995) 8577–8593.

[37] D. Poger, A.E. Mark, On the validation of molecular dynamics simulations of saturated and cis-monounsaturated phosphatidylcholine lipid bilayers: a comparison with experiment, J. Chem. Theory Comput. 6 (2010) 325–336.
[38] T.H. Schmidt, C. Kandt, LAMBADA & InflateGRO2: efficient membrane alignment and insertion of membrane proteins, J. Chem. Inf. Model. 52 (2012) 2657–2669.
[39] W. Humphrey, A. Dalke, K. Schulten, VMD: visual molecular dynamics, J. Mol. Graph. 14 (1996) 33–38 27–38.
[40] M. Raunest, C. Kandt, dxTuber: detecting protein cavities, tunnels and clefts based on protein and solvent dynamics, J. Mol. Graph. Model. (2011) 895–905.
[41] R.M. Epand, R.F. Epand, Functional consequences of the lateral organization of biological membranes, in: P.L. Yeagle (Ed.), The Structure of Biological Membranes, CRC Press, Taylor & Francis Group, Boca Raton, 2011, pp. 133–151.
[42] X. Cheng, I. Ivanov, H. Wang, S.M. Sine, J.A. McCammon, Molecular-dynamics simulations of ELIC—a prokaryotic homologue of the nicotinic acetylcholine receptor, Biophys. J. 96 (2009) 4502–4513.
[43] J. Gullingsrud, D. Kosztin, K. Schulten, Structural determinants of MscL gating studied by molecular dynamics simulations, Biophys. J. 80 (2001) 2074–2081.
[44] S. Khalid, P.J. Bond, S.S. Deol, M.S.P. Sansom, Modeling and simulations of a bacterial outer membrane protein: OprF from *Pseudomonas aeruginosa*, Proteins Struct. Funct. Bioinforma. 63 (2006) 6–15.
[45] B. Luan, R. Carr, M. Caffrey, A. Aksimentiev, The effect of calcium on the conformation of cobalamin transporter BtuB, Proteins Struct. Funct. Bioinforma. 78 (2010) 1153–1162.
[46] P. Pongprayoon, O. Beckstein, C.L. Wee, M.S.P. Sansom, Simulations of anion transport through OprP reveal the molecular basis for high affinity and selectivity for phosphate, Proc. Natl. Acad. Sci. 106 (2009) 21614–21618.
[47] T. Sun, M. Liu, W. Chen, C. Wang, Molecular dynamics simulation of the transmembrane subunit of BtuCD in the lipid bilayer, Sci. China Life Sci. 53 (2010) 620–630.
[48] D.P. Tieleman, M.S. Sansom, H.J. Berendsen, Alamethicin helices in a bilayer and in solution: molecular dynamics simulations, Biophys. J. 76 (1999) 40–49.
[49] C. Kandt, K. Gerwert, J. Schlitter, Water dynamics simulation as a tool for probing proton transfer pathways in a heptahelical membrane protein, Proteins 58 (2005) 528–537.
[50] C. Kandt, J. Schlitter, K. Gerwert, Dynamics of water molecules in the bacteriorhodopsin trimer in explicit lipid/water environment, Biophys. J. 86 (2004) 705–717.
[51] B. Luan, M. Caffrey, A. Aksimentiev, Structure refinement of the OpcA adhesin using molecular dynamics, Biophys. J. 93 (2007) 3058–3069.
[52] A.R. Braun, J.N. Sachs, J.F. Nagle, Comparing simulations of lipid bilayers to scattering data: the GROMOS 43A1-S3 force field, J. Phys. Chem. B 117 (2013) 5065–5072.
[53] C.J. Dickson, B.D. Madej, Ã.g.A. Skjevik, R.M. Betz, K. Teigen, I.R. Gould, R.C. Walker, Lipid14: the amber lipid force field, J. Chem. Theory Comput. 10 (2014) 865–879.
[54] J.P.M. Jämbeck, A.P. Lyubartsev, Derivation and systematic validation of a refined all-atom force field for phosphatidylcholine lipids, J. Phys. Chem. B 116 (2012) 3164–3179.
[55] B. Klasczyk, V. Knecht, Validating affinities for ion-lipid association from simulation against experiment, J. Phys. Chem. 115 (2011) 10587–10595.
[56] P. Prakash, R. Sankararamakrishnan, Force field dependence of phospholipid headgroup and acyl chain properties: comparative molecular dynamics simulations of DMPC bilayers, J. Comput. Chem. 31 (2010) 266–277.
[57] T. Huber, A.V. Botelho, K. Beyer, M.F. Brown, Membrane model for the G-protein-coupled receptor rhodopsin: hydrophobic interface and dynamical structure, Biophys. J. 86 (2004) 2078–2100.
[58] L.S. Caves, J.D. Evanseck, M. Karplus, Locally accessible conformations of proteins: multiple molecular dynamics simulations of crambin, Protein Sci. 7 (1998) 649–666.
[59] B. Das, V. Helms, V. Lounnas, R.C. Wade, Multicopy molecular dynamics simulations suggest how to reconcile crystallographic and product formation data for camphor enantiomers bound to cytochrome P-450cam, J. Inorg. Biochem. 81 (2000) 121–131.
[60] N. Fischer, C. Kandt, Three ways in, one way out: water dynamics in the transmembrane domains of the inner membrane translocase AcrB, Proteins 79 (2011) 2871–2885.
[61] N. Fischer, C. Kandt, Porter domain opening and closing motions in the multi-drug efflux transporter AcrB, Biochim. Biophys. Acta Biomembr. 1828 (2013) 632–641.
[62] C. Kandt, D.P. Tieleman, Holo-BtuF stabilizes the open conformation of the vitamin B12 ABC transporter BtuCD, Proteins 78 (2010) 738–753.
[63] C. Kandt, Z. Xu, D.P. Tieleman, Opening and closing motions in the periplasmic vitamin B12 binding protein BtuF, Biochemistry 45 (2006) 13284–13292.
[64] D.C. Koch, M. Raunest, T. Harder, C. Kandt, Unilateral access regulation: ground state dynamics of the *Pseudomonas aeruginosa* outer membrane efflux duct OprM, Biochemistry 52 (2013) 178–187.
[65] M. Raunest, C. Kandt, Locked on one side only: ground state dynamics of the outer membrane efflux duct TolC, Biochemistry 51 (2012) 1719–1729.
[66] K. Scherer, J.H. Spille, Grein, H.G. Sahl, U. Kubitscheck, unpublished results.
[67] A. Arkhipov, Y. Yin, K. Schulten, Four-scale description of membrane sculpting by BAR domains, Biophys. J. 95 (2008) 2806–2821.
[68] G.S. Ayton, P.D. Blood, G.A. Voth, Membrane remodeling from N-BAR domain interactions: insights from multi-scale simulation, Biophys. J. 92 (2007) 3595–3602.
[69] D.E. Chandler, J. Hsin, C.B. Harrison, J. Gumbart, K. Schulten, Intrinsic curvature properties of photosynthetic proteins in chromatophores, Biophys. J. 95 (2008) 2822–2836.
[70] R.O. Dror, R.M. Dirks, J.P. Grossman, H. Xu, D.E. Shaw, Biomolecular simulation: a computational microscope for molecular biology, Annu. Rev. Biophys. 41 (2012) 429–452.
[71] S.J. Marrink, D.P. Tieleman, Perspective on the Martini model, Chem. Soc. Rev. 42 (16) (2013) 6801–6822.
[72] G.A. Voth, Coarse-graining of Condensed Phase and Biomolecular Systems, 1 CRC Press, Taylor & Francis Group, Boca Raton, 2009.
[73] S.J. Marrink, M. Fuhrmans, H.J. Risselada, X. Periole, The MARTINI force field, in: G.A. Voth, G.A. Voth (Eds.), Coarse-Graining of Condensed Phase and Biomolecular Systems, 1, 2009.